

Supplementary information

Real-time imaging and elemental mapping of AgAu nanoparticle transformations

E. A. Lewis, T. J. A. Slater, E. Prestat, A. Macedo, P. O'Brien, P. H. C. Camargo and S. J. Haigh

Discussion of the oxidation mechanism

Assuming the starting material is a spherical particle 30 nm in diameter with composition Ag 96% Au 4%. The particle contains 1.375×10^{-18} moles of silver and has a surface area of $2.83 \times 10^{-15} \text{ m}^2$.

The flux of an ideal gas is given by

$$\Phi = \frac{P}{\sqrt{2\pi mkT}}$$

where P is the gas pressure, m is mass of the molecule, k the Boltzmann constant, and T the temperature. At a temperature of 293.15K and a pressure of 9×10^{-8} Torr (approximate column pressure in the microscope used in this work); the flux of O_2 molecules is $1.09 \times 10^{17} \text{ m}^{-2} \text{ s}^{-1}$.

This would result in 307 O_2 molecules s^{-1} hitting the surface of the 30 nm particle.

If every collision was successful (i.e. results in the generation of $2\text{Ag}_2\text{O}$), complete conversion of the particle to the oxide would require 673 s. However, the literature contains a number of studies of oxygen chemisorption on Ag and Au surfaces which suggest the probability of a successful collision is very low. The dissociative adsorption of O_2 on a clean Ag surface is believed to have a low sticking probability, between 10^{-3} and 10^{-5} .¹⁻³ The sticking probability of oxygen on gold is believed to be below 10^{-5} .⁴ Even if we use a generous value of 10^{-3} , a 30 nm particle would require ~187 hours to completely oxidise. As we see significant oxidation occurring in ~400 s (e.g. Figure S1), atmospheric oxygen clearly doesn't play a significant role in the oxidation process observed in this study.

We must therefore conclude that oxygen is not primarily supplied from the atmosphere but from the chemical species found on the surface of the nanoparticles and the surrounding region of substrate. The primary candidate is polyvinylpyrrolidone (PVP), a polymer employed in the nanoparticle synthesis which is found on the surface of the particles and deposited on the surrounding substrate during drop casting.⁵ It has previously been observed that electron beam irradiation of Co nanoparticles coated in the oxygen containing ligand lauric acid result in partial oxidation of the particles, forming cobalt oxide shells.⁶ However, this beam induced reaction didn't show the characteristic features of the Kirkendall effect, and in fact the beam induced shell formation was shown to inhibit *ex situ* Kirkendall hollowing.⁶ We propose that an analogous oxidation mechanism occurs here with the electron beam interacting with the PVP to generate reactive oxygen species. The electron beam is commonly observed to draw organic contamination into the scan area. This process allows additional PVP to be drawn to the particle from the surrounding substrate during imaging.

Supplementary Figures

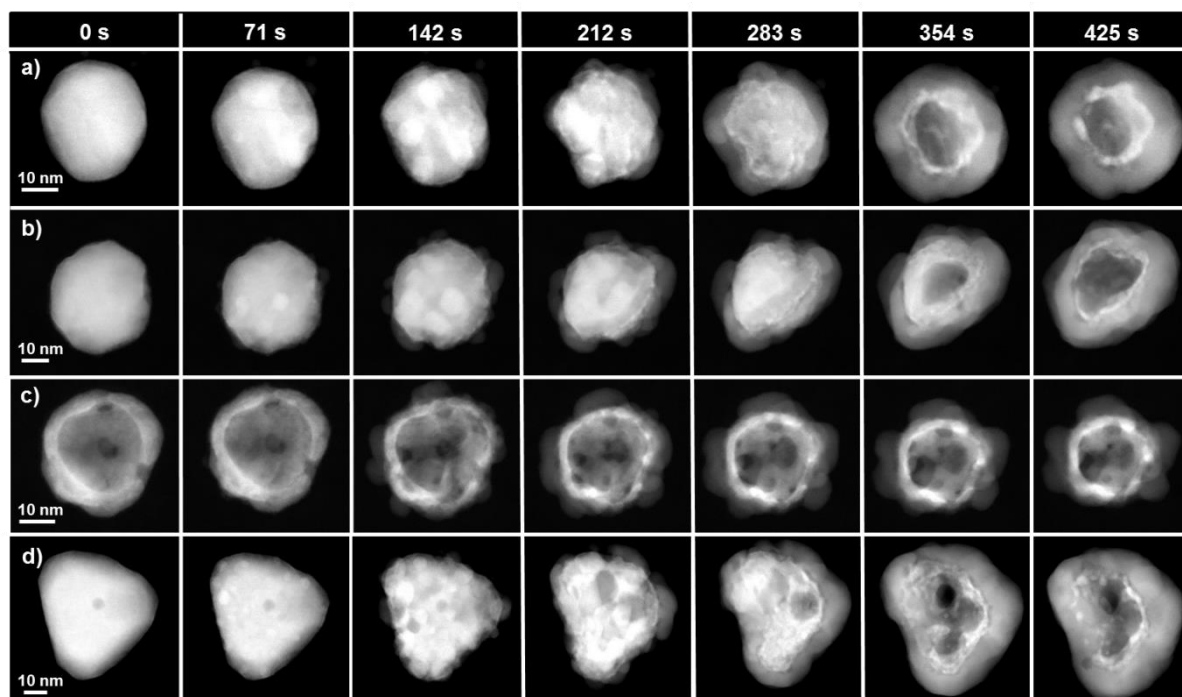


Figure S1. Shell growth and void formation are observed for a range of initial morphologies. Sequences of HAADF STEM images show the beam induced structural evolution of 5 particles. In all cases the particles were exposed to a constant dose rate of $\sim 2550 \text{ e}\text{\AA}^2\text{s}^{-1}$. All particles belong to the same sample of Ag-Au nanoparticles synthesised by the galvanic replacement reaction and containing $\sim 6\text{at.}\%$ Au $94\text{at.}\%$ Ag. While some particles (e.g. a and b) are solid and approximately spherical, other particles show some hollowing (c) or faceting (d) in their initial structure. Despite different initial morphologies a number of universal mechanistic features are observed during the beam induced reaction. Initially shell growth is non uniform, with islands of Ag₂O emerging on the particle's surface which eventually coalesce to form a complete shell. Shell growth is accompanied by the formation and growth of voids in the core. In some cases a single void grows in the particles core, in other cases several voids form initially before coalescing to form a single void.

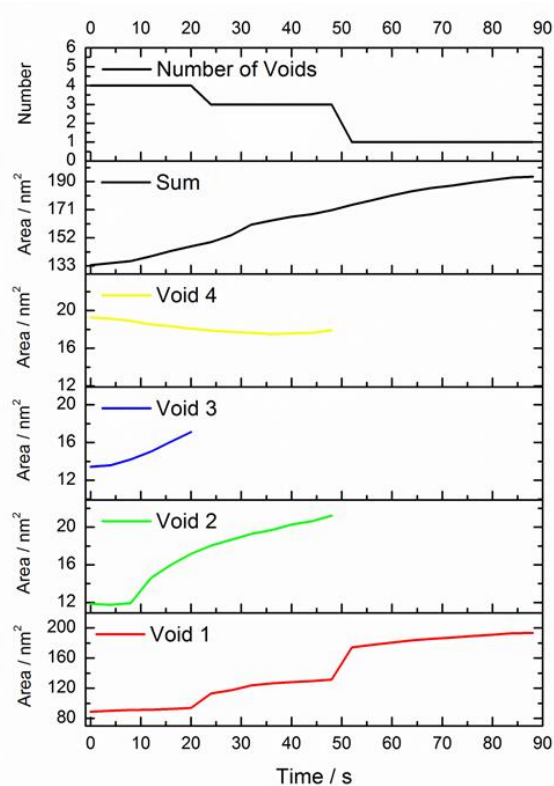
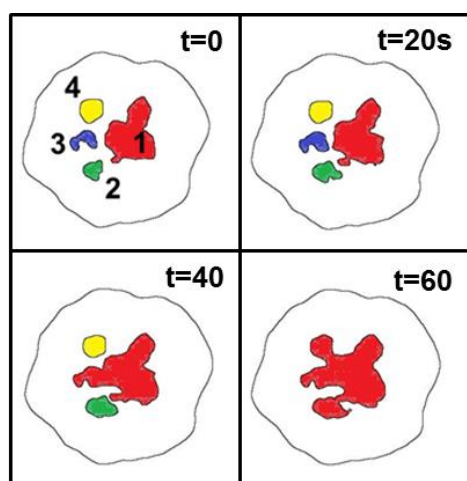


Figure S2. Quantitative analysis of void growth and coalescence. The nominal areas of the voids within a particle were measured with automated image thresholding. A self-consistent thresholding limit was applied to a series of 23 HAADF STEM images (Video S2) acquired as beam induced void growth and coalescence occurred. The particle studied is that shown in Figure 1. The total areal growth rate is found to remain approximately constant at $\sim 0.74 \text{ nm}^2\text{s}^{-1}$. However, the trajectories of individual voids are less predictable, for example void 4 doesn't increase in size at any point, shrinking before eventually coalescing with Void 1. The growth of Void 1 shows distinct jumps in size corresponding to the points where it consumes neighbouring voids.

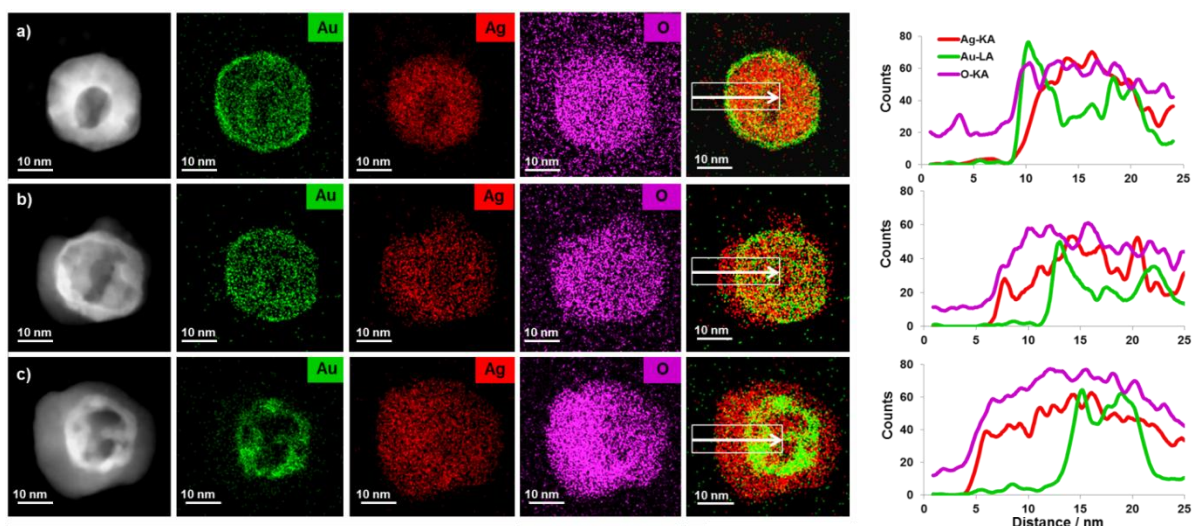


Figure S3. EDX spectrum imaging reveals growth of an Ag and O rich shell and inward diffusion of Au. EDX spectrum images of the same particles were recorded at different stages of the beam induced oxidation. (a) shows the particle before significant changes have occurred and (b) and (c) show later points of the beam induced reaction. Unlike the particle shown in Figure 1 this particle has some initial hollowing, this is a consequence of the galvanic replacement reaction used to synthesise the Ag-Au starting material. The spectrum images reveal that as the reaction proceeds, the area containing Ag grows. The Ag maps correlate strongly with the O maps suggesting the outward diffusion of Ag is driven by oxidation. Simultaneously the area containing Au decreases, it is believed that inward diffusion of Au occurs due to the increased concentration of vacancies in the core which accompanies the outward diffusion of Ag. Throughout this process the Ag:Au ratio remains constant (94at.% Ag, 6at.% Au) however, the amount of oxygen present (O/Ag at.% ratio) increases ~137% between (a) and (c), further supporting the oxidation hypothesis. The growth of an Ag_2O shell and the inward diffusion of Au are further demonstrated by the line scans shown in the right hand column.

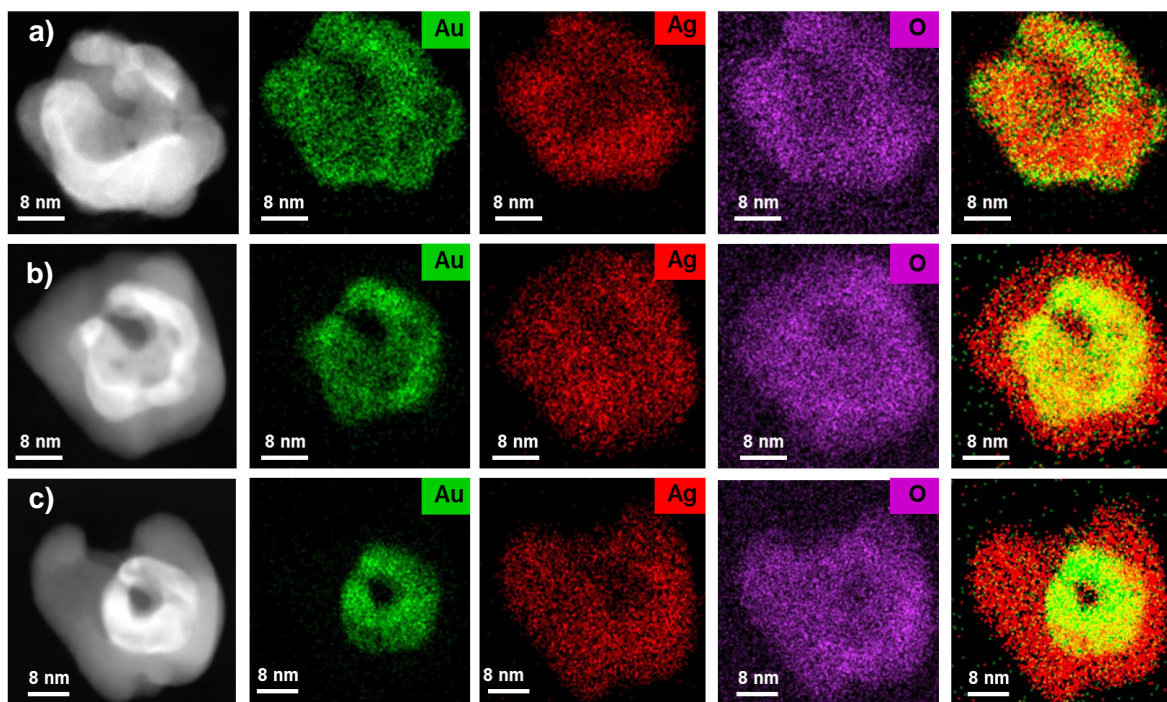


Figure S4. The lattice resolution images in Figure 3 confirm that shell growth is due to Ag_2O formation. EDX spectrum images acquired for the particle shown in Figure 3 at various stages of the beam induced reaction show the changes in elemental distribution that accompany the formation of Ag_2O . The changing distributions of Ag, Au and O are similar to those seen in Figures 1 and S3, with Ag diffusing outwards while Au diffuses inwards and a strong correlation between the distributions of Ag and O.

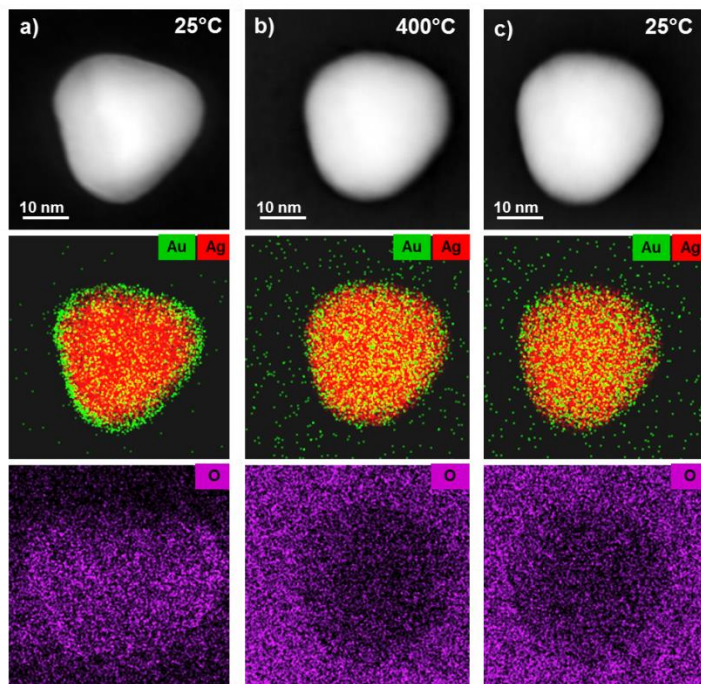


Figure S5. Oxidation is substrate dependent. Upon heating to 400°C particles on amorphous carbon immediately alloy. However, after quenching, no beam induced restructuring occurred when exposed to the same dose rates that caused the transformations shown in Figures 1 and 4. The absence of void formation and hollowing cannot be attributed to a shortage of oxygen; quantification of spectrum images reveals that O/Ag at.% ratio increased 622% from an initial value of 0.67 (a) to a final value of 4.82 (c) (probably a result of the electron beam drawing PVP to the scan area) while the Ag: Au ratio remains constant at 97at.% Ag 3at.% Au. In fact, the final O/Ag ratio is actually considerably higher than that seen in comparable examples where reactions have occurred on Si_3N_4 grids (e.g. in Figure 1 the final ratio is 2.18), but despite more oxygen accumulating in the scanned area during imaging there is no evidence of shell growth and hollowing. Mapping the oxygen counts reveals that, in contrast to samples on Si_3N_4 (where O and Ag counts are clearly correlated), the support surrounding the particles contains more O than the area occupied by the AgAu particle. It is therefore postulated that the amorphous carbon support reacts preferentially with oxygen containing species, preventing Ag_2O formation.

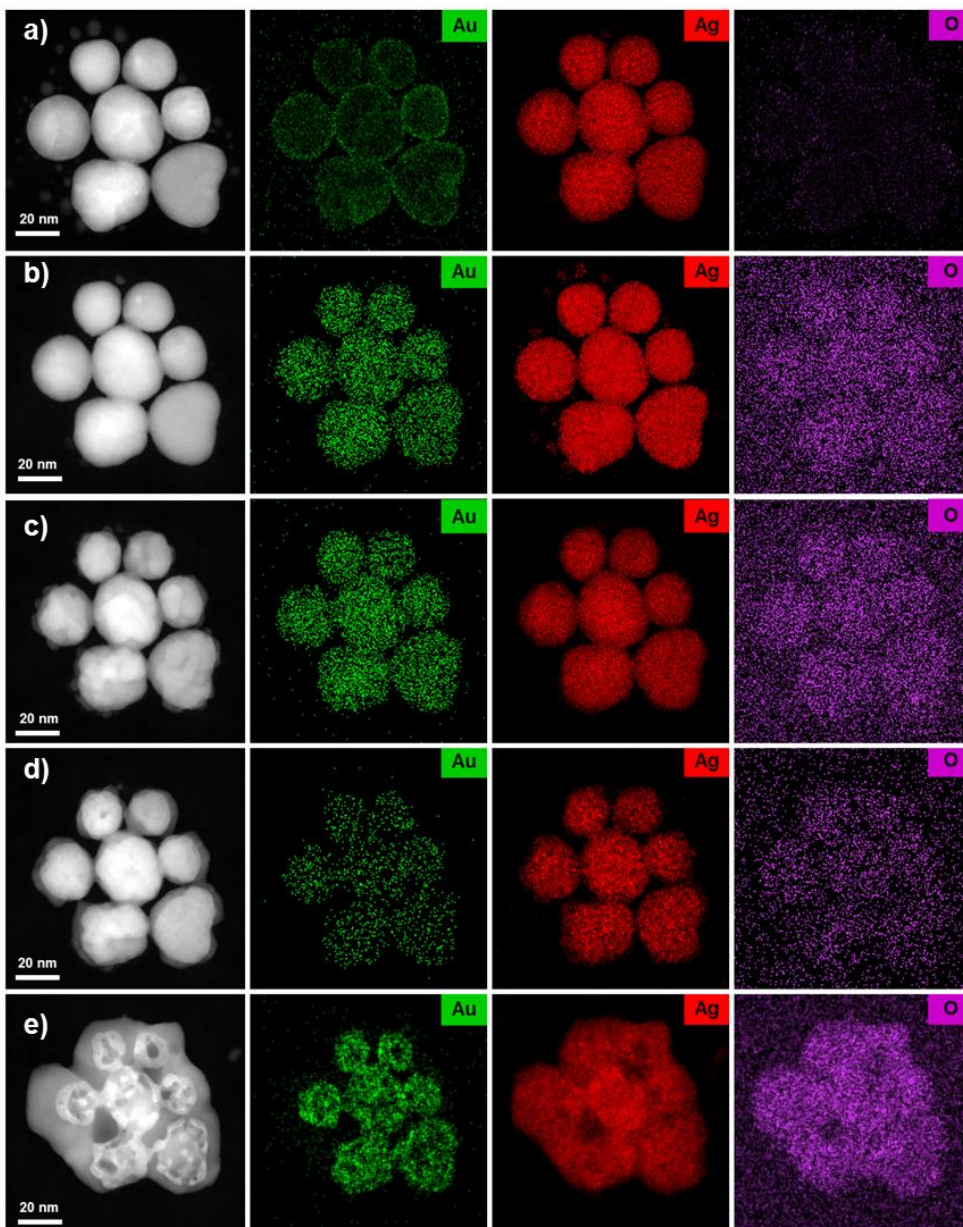


Figure S6. Elemental maps corresponding to figure 4. (a) shows the initial Au surface segregated particles, (b) shows the homogeneously alloyed AgAu particles formed by heating to 400°C, (c-e) show the different stages of the beam induced shell growth and hollowing that occurs after quenching to room temperature. The maps of O and Ag counts for (e) suggest that the increase in oxygen counts (Figure 4f) that accompanies the beam induced reaction is due to the growth of an Ag₂O shell.

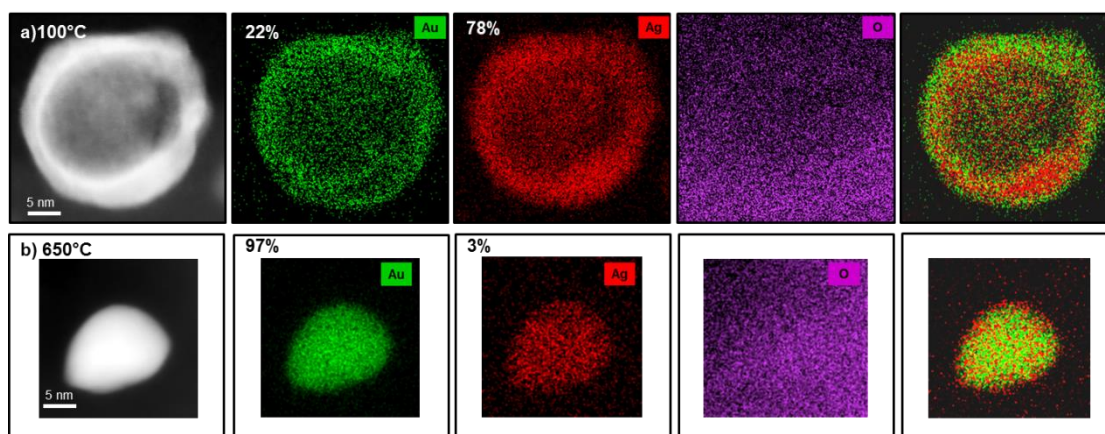


Figure S7. Heating Au surface segregated particles to 400°C results in alloying and some morphological changes (rounding of faceted edges and some loss of hollowing), however, the size and shape of the particle is largely retained and the ratio of Ag:Au remains identical to that measured at room temperature. In contrast, we observe a dramatic change in particle size, shape, and composition upon heating to 650°C. The particle shown in this figure shrinks dramatically upon heating, EDX quantification reveals that this shrinkage corresponds to a dramatic loss of Ag. The particle is initially 78at.% Ag 22at.% Au (coming from a different sample to the lower Au content particles used elsewhere in this paper) but the heated particle is 3at.% Ag 97at.% Au. This is consistent with previous reports which show that at high temperatures the lower melting point component of a bimetallic nanoparticle system will leech out, improving the particles' high temperature stability.⁷ The melting points of bulk Ag and Au are 961.8°C and 1064°C respectively but nanoparticles show significant melting point depression. Pure Ag particles of a similar size to those studied here have been observed, by *in situ* TEM heating experiments, to sublime at 600-700°C.⁸

Supplementary Videos

Video S1. Video of early stages of growth. Video comprised of a sequence of HAADF STEM images capturing the particle shown in Figure 1 during the early stages of the beam induced reaction. This video covers the period between the images shown Figures 1a and 1c. The particle is subjected to a constant dose rate of $\sim 4990 \text{ e}\text{\AA}^2\text{s}^{-1}$ during the entire video. The Ag_2O shell appears to emerge from at least 3 distinct sites upon the particle's surface. The video clip, available in the electronic supplementary material, plays at 4x real speed.

Video S2. Video of void coalescence. Video comprised of a sequence of HAADF STEM images showing the growth and coalescence of voids in the particle shown in Figure 1. This video covers the period between the images shown Figures 1d and 1e. The particle is subjected to a constant dose rate of $\sim 4990 \text{ e}\text{\AA}^2\text{s}^{-1}$ during the entire video. By this point in the growth trajectory, the multiple Ag_2O islands seen in Video S1 have combined to form a complete shell and multiple voids have formed in the core. As the beam induced reaction proceeds the voids continue to grow and eventually coalesce. A quantitative analysis of this image sequence can be found in supplementary Figure S2. The video clip, available in the electronic supplementary material, plays at 4x real speed.

Video S3. Video comprised of a sequence of HAADF STEM images showing shell growth and void formation in a cluster of alloyed AgAu nanoparticles. This video covers the period between the images shown in Figures 4d and 4e. The particles were exposed to a constant dose rate of $\sim 2550 \text{ e}\text{\AA}^2\text{s}^{-1}$. Particles alloyed by heating undergo a beam induced reaction after they are returned to room temperature. This reaction shows similar characteristics to the reaction observed in Au surface segregated particles. However, the proximity of particles to other particles undergoing the same beam induced reaction influences the final morphology, with the growing shells of neighbouring particles contacting and merging. The video clip, available in the electronic supplementary material, plays at ~ 9 x real speed.

Supporting References

1. P. J. Goddard and R. M. Lambert, *Surface Science*, 1981, **107**, 519-532.
2. G. Rovida and F. Pratesi, *Surface Science*, 1975, **52**, 542-555.
3. W.-X. Li, C. Stampfl and M. Scheffler, *Physical Review B*, 2003, **67**, 045408.
4. N. D. S. Canning, D. Outka and R. J. Madix, *Surface Science*, 1984, **141**, 240-254.
5. T. J. A. Slater, A. Macedo, S. L. M. Schroeder, M. G. Burke, P. O'Brien, P. H. C. Camargo and S. J. Haigh, *Nano Letters*, 2014, **14**, 1921-1926.
6. Z. Yang, M. Walls, I. Lisiecki and M.-P. Pileni, *Chemistry of Materials*, 2013, **25**, 2372-2377.
7. A. Cao and G. Vesper, *Nature Materials*, 2010, **9**, 75-81.
8. M. A. Asoro, D. Kovar and P. J. Ferreira, *ACS Nano*, 2013, **7**, 7844-7852.